Comprehensively modeling and parametric identification for speed prediction of L1B2 ultrasonic motor

Yang Deng[1], Gang Zhao[1], Xingyu Yi[1] and Wenlei Xiao[1*]

[1]School of Mechanical Engineering and Automation, Beihang University, Beijing, China

[*]Corresponding author's e-mail: xiaowenlei@buaa.edu.cn

Abstract. Ultrasonic motor is a kind of newly developed motor different from the traditional electromagnetic one, with its output is obtained by inverse piezoelectric effect and ultrasonic oscillation. As it is a complex coupling system, speed control of the motor is a quite difficult task. A comprehensive parametric model for prediction of the steady-state speed of a linear ultrasonic motor is developed in this paper. The model is derived from synthesizing coupled subsystem models, and retains physical insight into some important nonlinearities. The driving circuit employing H-bridge inverter and LC resonance is described. The vibration equations of the stator are deduced by using Hamilton's principle. An interface friction model involving asperity based stick behavior is introduced to characterize the stick-slip-separation dynamics at the interface. Further, an effective real-time and synchronous data acquisition and transmission experimental setup based on a L1B2 ultrasonic motor actuated motion platform is established to collect data for the parametric identification, and the results validate reliability of the model.

1. Introduction

Ultrasonic motors (USMs) with the excellent features of high accurate, quick response and low noise, have been widely used in precise positioning and actuating [1]. Among them the linear ultrasonic motor (LUSM), which converts micro ultrasonic oscillation into macro linear motion, has been of great interest. However, due to that the LUSM is a complicated coupling system, it is difficult to implement the speed prediction and control [2]. For the subsystem of driving circuit, frequency-drift and temperature-drift compensating techniques are needed. The subsystem of contact mechanism relates many factors such as material features, roughness and preload, and it greatly affects the speed. And the contact behavior of LUSM has strong position-dependent nonlinearity compared with other types of USMs. Also, comprehensively modeling of the whole motor is also a hard task. For high-performance control, the model should not be too complex or inaccessible and should retain physical insight into some important nonlinearities. Thus, neither pure analytical nor pure black-box identification methods can be used.

L1B2 USM is a bimodal LUSM that belongs to a kind of standing wave type USMs (SWUMs), the stator and the slider of which are in intermittent contact. Many studies on modeling are carried out. A dynamic model including four subsystems is developed in which the interface friction is simplified as Coulomb model [3]. On contact mechanism, Hertz microscopic contact model [4] and asperity based model [5] are used. However, these analytical models are too complex and failed to describe the position-dependent nonlinearity. And none concludes a comprehensive model. By modern identification and artificial intelligence methods, black-box models are obtained without any prior knowledge, but of poor precision in cases of system state changing and complex state space relationships [6, 7].

This paper proposes a new parametric model of the whole motor system to predict the steady-state output speed of L1B2 USM with considering the position-dependent nonlinearity.

2. Description of L1B2 USM and the test rig

The schematic of motor investigated is given below. It consists of a piezoelectric resonator, a driving tip, a preload spring and a fixture. The first longitudinal and second bending modes are simultaneously excited by applying sinusoidal or cosine signal to CH1 or CH2 to produce elliptical motion. The test rig includes a prototype motor, a bolt to adjust the initial preload, a friction bar, a linear guide and an encoder.

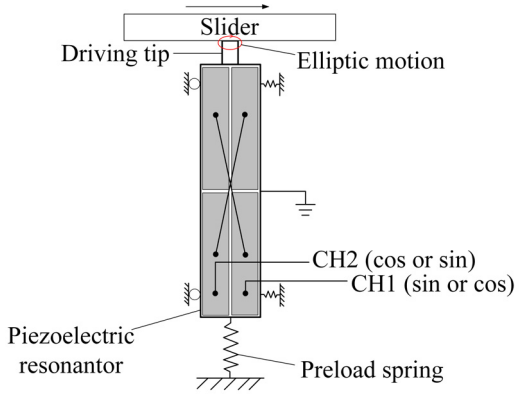

Figure 1. The schematic of L1B2 USM

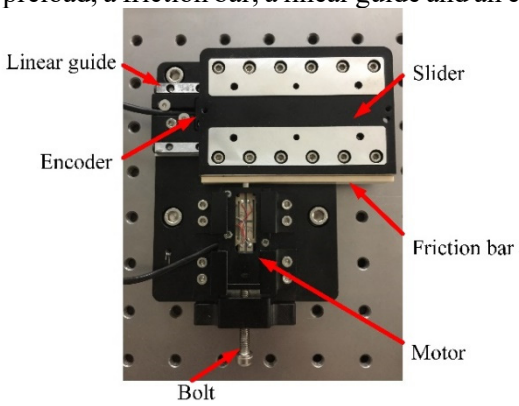

Figure 2. The motor based test rig

3. Subsystem models

The four coupled subsystems is shown below. Here we consider the steady-state response of the model to study its changes with the position of the interface contact point on friction bar.

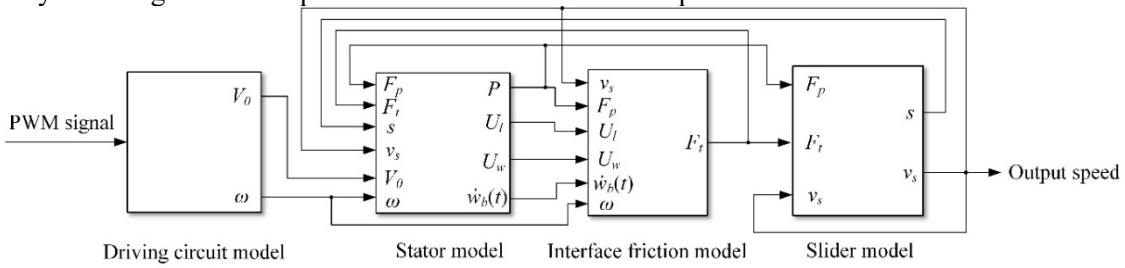

Figure 3. The steady-state model of L1B2 USM

3.1. The driving circuit

The electric drive employs H-bridge inverter and LC resonance. With the PWM control signal, the resulted square wave voltage V_{inv} derived from the current voltage supply V_s acts as input for the resonance. And by LC resonance, the sinusoidal output of the drive with amplitude V_0 and frequency ω can be obtained. By using Fourier transform, the fundamental component of V_{inv} is given by [3]

$$V_{\text{invb}} = 4\pi^{-1}\sin(0.5\pi\delta)V_s \sin\omega_s t, \tag{1}$$

where δ is duty ratio of the PWM signal and ω_s is switching frequency. Usually ω_s=ω and they are close to the resonant frequency of the stator. Equivalent circuit for the resonance tank is shown below.

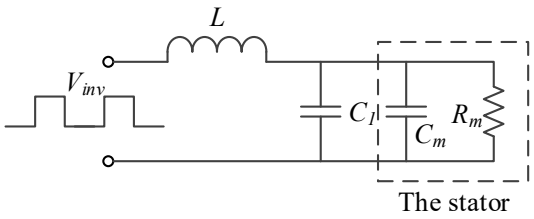

Figure 4. The equivalent circuit of the resonance tank

The inductor L and the capacitance C_1 can be determined by matching technique. The amplitude of the sinusoidal output can be obtained by (ω_0 is the resonant frequency)

$$V_0 = 4\pi^{-1}\sin(0.5\pi\delta)V_s R_m^{-1}\sqrt{R_m^2+\omega_0^2 L^2}, \tag{2}$$

$$\omega_0 = \sqrt{L^{-1}C^{-1}-R_m^{-2}C^{-2}}, C = C_1 + C_m, \tag{3}$$

Practically, the electrical parameters of L and C_1 are affected by frequency ω_s or temperature T,

$$L = L(T,\omega_s), C_1 = C_1(\omega_s), \tag{4}$$

3.2. The stator

The rectangle stator is considered as a Timoshenko beam and vibration displacement components are

$$u(x,t) = \phi_u(x)u_l(t), w(x,t) = \phi_b(x)w_b(t), \tag{5}$$

in which $u(x,t)$ and $w(x,t)$ are the displacements in longitudinal and transverse directions. And $\phi_u(x)$, $\phi_b(x)$ are the mode shape functions. By using Hamilton's principle, the vibration equations are

$$M_l\ddot{u}_l(t) + C_l\dot{u}_l(t) + K_l u_l(t) = A_l V_0 \sin\omega t + \eta_N F_N, \tag{6}$$

$$M_b\ddot{w}_b(t) + C_b\dot{w}_b(t) + K_b w_b(t) = A_b V_0 \sin\omega t + \eta_T F_T, \tag{7}$$

where M_l and M_b, C_l and C_b, K_l and K_b are the mass, damping and stiffness for the L1 mode and the B2 mode, respectively. A_l and A_b are the corresponding electromechanical coupling factors. η_N and η_T are the load coefficients for normal interface force F_N and tangential interface force F_T.

In order to describe the position-dependent nonlinearity, a vibration related nominal axial force of the stator P is introduced as a function of the position s. Accordingly, the mode shape functions are

$$\phi_u(x) = \cos\pi x / L, \tag{8}$$

$$\phi_b(x,P) = C\cos\beta_1(P)x + D\sin\beta_1(P)x + E\sinh\beta_2(P)x + F\cosh\beta_2(P)x, \tag{9}$$

$$\beta_1^2 = \left[\left(\frac{P}{2EI}\right)^2 + \frac{\rho S}{EI}\omega_b^2\right] - \frac{P}{2EI}, \tag{10}$$

$$\beta_2^2 = \left[\left(\frac{P}{2EI}\right)^2 + \frac{\rho S}{EI}\omega_b^2\right] + \frac{P}{2EI}, \tag{11}$$

where $L, E, I, \rho, S, \omega_b$ are length of stator, Young's modulus, moment of inertia, density, cross section area and natural frequency of B2 mode, respectively. The steady-state vibration amplitudes are

$$U_l = F_l\phi_u(L)\left(K_l\sqrt{\left(1-\left(\omega/\omega_{l0}\right)^2\right)^2 + \left(2\zeta_l\omega/\omega_{l0}\right)^2}\right)^{-1}, \tag{12}$$

$$U_w = F_b\phi_b(L)\left(K_b\sqrt{\left(1-\left(\omega/\omega_{b0}\right)^2\right)^2 + \left(2\zeta_b\omega/\omega_{b0}\right)^2}\right)^{-1}, \tag{13}$$

where F_l, F_b denote the amplitudes of equivalent harmonic excitations for the L1 and B2 modes, and $\omega_{l0} = \sqrt{K_l/M_l}, \omega_{b0} = \sqrt{K_b/M_b}, \zeta_l = C_l/2M_l\omega_{l0}, \zeta_b = C_b/2M_b\omega_{b0}$.

$$F_l = A_l V_0 + \alpha_l \eta_N F_p, F_b = A_b V_0 + \alpha_b \eta_T F_t, \tag{14}$$

in which F_p, F_t are the static axial force and the steady-state thrust respectively and α_l, α_b are the corresponding nonnegative equivalent factors.

$$F_p = \frac{1}{T}\int_t^{t+T} F_N dt, F_t = \frac{1}{T}\int_t^{t+T} F_T dt, \tag{15}$$

$$F_p = \alpha_0 P, \tag{16}$$

where T is the period time and α_0 is a nonnegative conversion factor satisfying $\alpha_0 \neq 1$. With the analysis of the intermittent contact mechanism, the normal interface force in one period can be given as

$$F_N = \begin{cases} 0, & 0 < \omega t < (\pi - \varphi_c)/2, (\pi + \varphi_c)/2 < \omega t < 2\pi \\ k_e U_l (\sin \omega t - \cos 0.5\varphi_c), & (\pi - \varphi_c)/2 \le \omega t \le (\pi + \varphi_c)/2 \end{cases} \tag{17}$$

in which k_e is the equivalent contact stiffness of friction layer. The relationship between φ_c and F_p is

$$\left(\sin 0.5\varphi_c - 0.5\varphi_c \cos 0.5\varphi_c\right) U_l = \pi F_p / k_e \tag{18}$$

Different from one-to-one mapping between P and s, mapping between the transverse vibration amplitude U_w and the position s is one-to-multiple under different input voltages.

3.3. The interface friction

For the micro contact friction mechanism, the effect of the asperity cannot be ignored. The developed stick-slip interface friction model is shown in Figure 5. In the stick phase, the friction force is determined by the elastic-plastic deformation of asperity links and is proportional to the relative displacement. In the slip phase, with break of the pairs of the asperity links and newly formed lubricating film, the friction force contains dynamic friction force and viscous friction force. The threshold of the relative displacement for the two phases is denoted by u_m and the interface friction forces are as follows

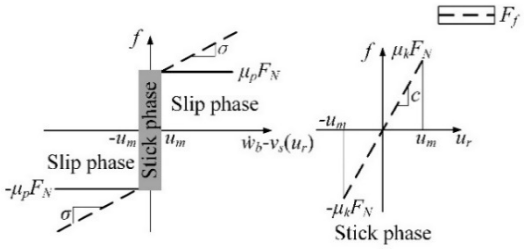

Figure 5. The schematic of the stick-slip interface friction model

$$F_f = \begin{cases} \mu_k F_N, \dot{w}_b(t) \ge v_s, |u_r(t)| \le u_m \\ -\mu_k F_N, \dot{w}_b(t) < v_s, |u_r(t)| \le u_m \end{cases}, \mu_k = c|u_r|, \tag{19}$$

$$F_f = \begin{cases} \sigma(\dot{w}_b - v_s) + \mu_p F_N, \dot{w}_b(t) \ge v_s, |u_r(t)| > u_m \\ \sigma(\dot{w}_b - v_s) - \mu_p F_N, \dot{w}_b(t) < v_s, |u_r(t)| > u_m \end{cases}, \tag{20}$$

in which σ is the viscous friction coefficient and v_s is the steady-state speed of the slider. And μ_k is the friction coefficient in the stick phase that is proportional to the magnitude of relative displacement. And μ_p is the dynamic friction coefficient. The proportional coefficient c is given by $c = \mu_p / u_m$.

Figure 6 shows the relationship between $\dot{w}_b(t)$ and v_s in one period.

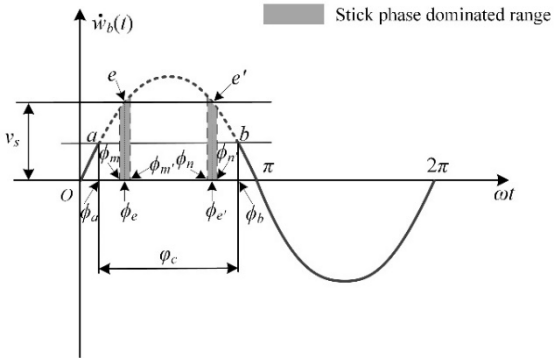

Figure 6. The relationship between transverse vibration velocity of the stator and steady-state speed of the slider in one period

3.4. The slider

The motion equation of the slider is obtained by force equilibrium as follows

$$m\frac{dv_s}{dt}+c_r v_s = F_d + F_g - F_{load}, \tag{21}$$

$$F_g = \text{sign}(-v_s)\mu_{sd}(F_p + 9.81m), \tag{22}$$

where m, c_r, μ_{sd} are the mass of slider, viscous damping coefficient, and dynamic friction coefficient of linear guide and F_d, F_{load} are the driving the load forces. The friction force F_g includes the effects of gravity force of the slider and normal interface force that is time-averaging of the static axial force F_p.

4. Comprehensively modeling and parametric identification

For simplification, the submodel of driving circuit is not included. The feedback position and speed of the slider s and v_s act as state input for the model in the present moment. The input voltage with V_0 and ω act as excitation input, and the output is the speed of slider to be predicted in the next moment.

Here we consider the case of high-voltage input. According to Section 3.3, the interface friction can be approximated by pure slip friction in this case. On the assumption that the contact angle is a constant, i.e., $\varphi_c = \pi$, by employing Fourier transform the fundamental component of interface friction force is

$$F_{fb} = \left[0.5\sigma\omega U_w - 2\pi^{-1}\sigma v_s + \mu F_p\left(\sin 2\omega t_1 + 0.5\pi - 2\omega t_1\right)\right]\sin\omega t, \tag{23}$$

where $t_1 = \omega^{-1}\arcsin\left(v_s\omega^{-1}U_w^{-1}\right)$ and the steady-state transverse vibration amplitude is

$$U_w = \left[A_b V_0 - 0.5\eta_T\sigma\omega U_w + 2\eta_T\pi^{-1}\sigma v_s - \eta_T\mu F_p\left(2v_s\omega^{-1}U_w^{-1}\sqrt{1-v_s^2\omega^{-2}U_w^{-2}} - 2\arcsin\left(v_s\omega^{-1}U_w^{-1}\right) + 0.5\pi\right)\right]$$

$$\cdot\left(-\phi_b(L)\right)K_b^{-1}\left(\left(1-\left(\omega/\omega_{b0}\right)^2\right)^2 + \left(2\zeta_b\omega/\omega_{b0}\right)^2\right)^{-1/2}, \tag{24}$$

An interesting phenomenon is observed in experiment that v_s is approximately proportional to ωU_w. The solution of U_w can be obtained below (k_0 denotes the proportional coefficient)

$$U_w = \left[A_b V_0 + 2\eta_T\pi^{-1}\sigma v_s - \eta_T\mu\left(2k\sqrt{1-k_0^2} - 2\arcsin k_0 + 0.5\pi\right)F_p\right]\left(\Theta^{-1} + 0.5\eta_T\sigma\omega\right)^{-1}, \tag{25}$$

$$\Theta = \left(-\phi_b(L)\right)K_b^{-1}\left(\left(1-\left(\omega/\omega_{b0}\right)^2\right)^2 + \left(2\zeta_b\omega/\omega_{b0}\right)^2\right)^{-1/2}, \tag{26}$$

Based on the difference representation of Equation (21), output speed is obtained by

$$F_d = \frac{1}{T}\int_0^T F_f dt, \tag{27}$$

$$v_s(k+1) = \left(1 - c_r T_s / m\right) v_s(k) + T_s / m\left(F_d(k) + F_g(k) - F_{load}(k)\right), k = 0,1,2,\ldots \tag{28}$$

in which T_s is the sampling time. And the above difference equation can be expanded as

$$\begin{aligned} v_s(k+1) = &\left[1 - c_r T_s / m + \sigma / m\left(\mathrm{A}(k) - 0.5T_s\right)\right] v_s(k) + \mathrm{B}(k) / m V_0(k) \\ &+ \mu F_p(k) / m\left[-0.5\pi \mathrm{A}(k)\left(2k_0\sqrt{1-k_0^2} - 2\arcsin k_0 + 0.5\pi\right) + T_s\left(2\sqrt{1-k_0^2} - 1\right)\right] \\ &- T_s / m\left[9.81 m_{load}(k) - sign\left(-v_s(k)\right)\mu_{sd}\left(9.81 m_s + 0.5F_p(k)\right)\right], \end{aligned} \tag{29}$$

$$\mathrm{A} = 4\pi^{-1}T^{-1}\sigma\eta_T T_s / \left(\Theta^{-1} + 0.5\sigma\omega\eta_T\right),\ \mathrm{B} = 2T^{-1}\sigma A_b T_s / \left(\Theta^{-1} + 0.5\sigma\omega\eta_T\right), \tag{30}$$

Here, nonlinear polynomial models of the position are introduced for $P, \mathrm{A}, \mathrm{B}$ (n, p, q are orders)

$$P = P_n(s), \mathrm{A} = \mathrm{A}_p(s), \mathrm{B} = \mathrm{B}_q(s), \tag{31}$$

Here the parametric identification is implemented by using off-line maximum likelihood estimation.

$$\frac{\partial J}{\partial \boldsymbol{\theta}} = -\sum_{k=1}^{N}\left(\frac{\partial y(t_k)}{\partial \boldsymbol{\theta}}\right)^T R^{-1}\left[z(t_k) - y(t_k)\right] = 0, \tag{32}$$

where J is the fitness function, and R is the covariance between prediction $y(t_k)$ and measured $z(t_k)$. $\boldsymbol{\theta}$ is the parameter vector to be identified and above equation can be resolved by iteration algorithm.

5. Simulation and experimental results

5.1. Experimental setup

The schematic and physical layout of the experimental setup are illustrated below. The encoder used in the L1B2 USM test rig has a resolution of 50nm. A PZT-8 cube of dimensions 30mm×7.5mm×3mm is chosen as the stator. A laser vibrometer (OFV-503/2510, Polytec, Inc. Germany) is used to collect the vibration data, and a data acquisition card (DAQ card) with the maximum sampling rate of 2MS/s (USB-6361, NI, Inc. USA) along with NI-DAQmx software in LABVIEW environment are employed for real-time data monitoring and storage. A servo drive supporting EtherCAT technology, is designed and communicates with host PC by TwinCAT software. The load is applied by mechanism of fixed pulley. And the overall setup is placed on a pneumatic vibration isolation table (T1020CK, Thorlabs, Inc. USA).

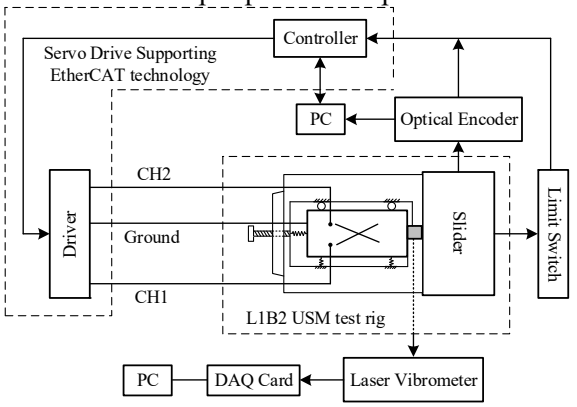

Figure 7. The schematic of the experimental setup

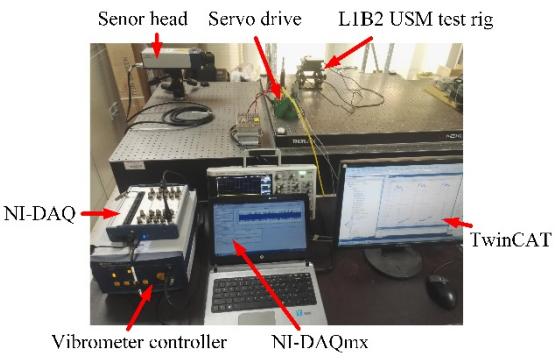

Figure 8. The physical layout of the setup

The driving frequency is set to be a constant of 48.5kHz. Figure 9(a) shows that the load-free steady-state speed of the slider varies with the position under different inputs and Figure 9(b) shows the effect of the horizontal load on the speed under a constant input. Figure 9(c) shows the discrete points of $(\omega U_w, v_s)$, and the fitting line indicates that v_s has significantly positive linear relationship to ωU_w.

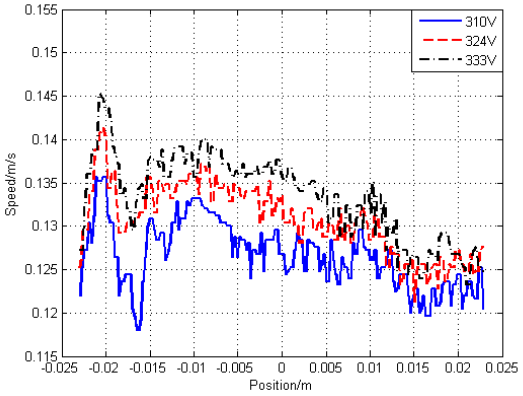

(a) Variation of load-free steady-state speed with position under different high-voltage inputs

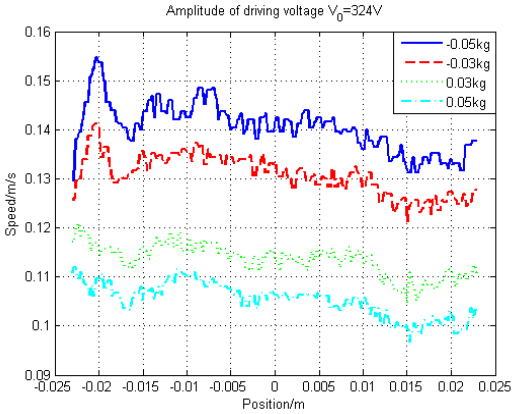

(b) Variation of steady-state speed with position under different horizontal loads with $V_0 = 324\text{V}$

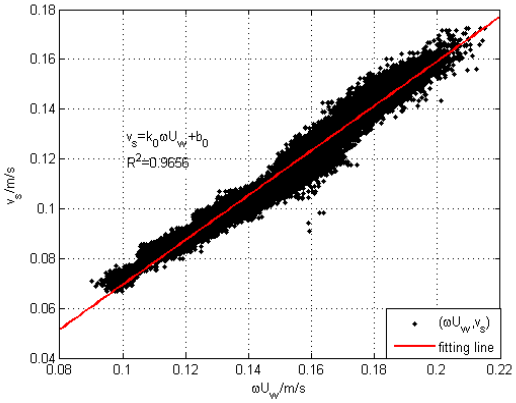

(c) The relationship between the steady-state speed and the amplitude of the transverse vibration velocity

Figure 9. The measured experimental data

5.2. Simulation and model validation

Based on Section 4, input and output vectors of the comprehensive model are given by

$$\boldsymbol{x} = [V_0 \quad s \quad v_s]^T, y = v_s, \tag{33}$$

The weights sampled from 0.03kg to 0.09kg with an equal interval of 0.02kg are applied as the loads. The models in Equation (31) are represented by eight-order polynomials of the position.

$$P = \boldsymbol{p}^T \boldsymbol{S}, \mathrm{A} = \boldsymbol{\alpha}^T \boldsymbol{S}, \mathrm{B} = \boldsymbol{\beta}^T \boldsymbol{S}, \tag{34}$$

where $\boldsymbol{p}, \boldsymbol{\alpha}, \boldsymbol{\beta}$ are coefficient vectors of the polynomials, and $\boldsymbol{S}$ is eight-order vector of the position.

The parameter vector to be identified can be represented as

$$\boldsymbol{\theta} = [c_r \quad \sigma \quad \mu \quad k_0 \quad \mu_{sd} \quad \boldsymbol{\alpha} \quad \boldsymbol{\beta} \quad \boldsymbol{p}]^T, \tag{35}$$

By empolying the global search toolbox in MATLAB, the identification result for the model is listed.

Table 1. Estimation result of parameters in the comprehensive model

Parameters to be identified	$c_r(N\cdot s/m)$	$\sigma(N\cdot s/m)$	$\mu(1)$	$k_0(1)$	$\mu_{sd}(1)$
Estimation result	3.0871	0.0014	0.2297	0.5844	0.0994

$\boldsymbol{\alpha}=[-2.2549\times10^{-6}\ \ -0.8633\ \ -63.5158\ \ 31.9521\ \ 81.9674\ \ -132.9991\ \ -1.3819\ \ 0.0078\ \ 5.9610\times10^{-4}]^T$

$\boldsymbol{\beta}=[8.3913\times10^{7}\ \ -8.7852\times10^{6}\ \ -1.5375\times10^{5}\ \ 7.2194\times10^{3}\ \ 76.8995\ \ -1.7187\ \ -0.0104\ \ 6.7924\times10^{-5}\ \ 1.0573\times10^{-6}]^T$

$\boldsymbol{p}=[-1.0573\times10^{14}\ \ -3.1504\times10^{12}\ \ 1.4224\times10^{11}\ \ 2.9068\times10^{9}\ \ -2.5863\times10^{7}\ \ -7.8668\times10^{5}\ \ -1.9848\times10^{4}\ \ 59.4874\ \ 6.0554]^T$

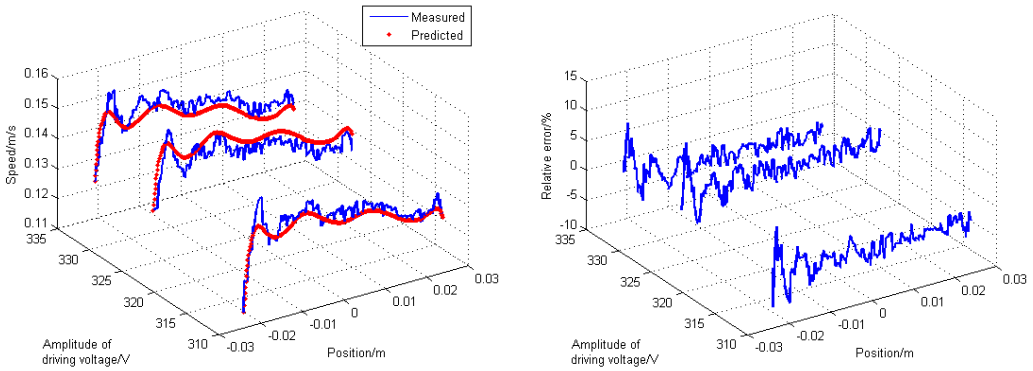

(a) Comparsion between the predicted and the measured with the load of -0.05kg

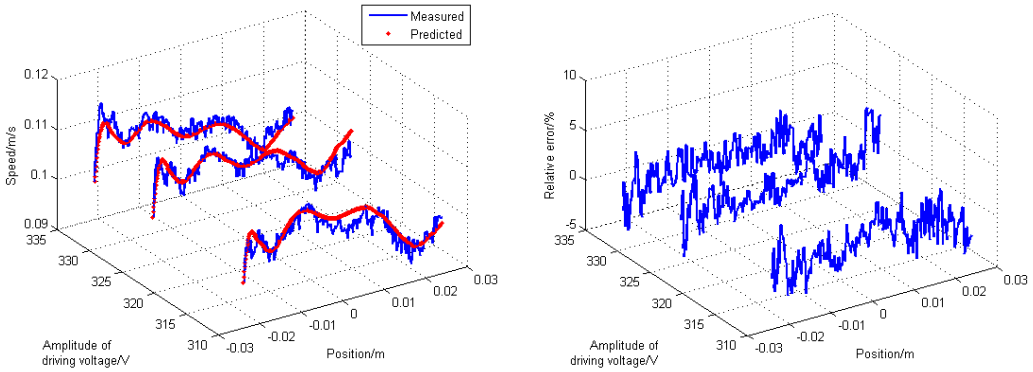

(b) Comparsion between the predicted and the measured with the load of 0.05kg

Figure 10. Comparison between the model output and the experimental data

The loads of ±0.05kg are chosen to be the testing data set, and the results are shown in Figure 10. It the noted that the absolute values of the relative error are within 5% in almost all the positions except for the possible large fluctuations at two edges positions, which may result from the disturbtion by collision between the linear guide and the mechanical limit screw.

6. Conclusion

In the paper, a new parametric comprehensive model is presented for steady-state speed prediction and control for L1B2 USM, in which both analytical techniques and identification methods are employed to cover the uncertain and complicated position-dependent nonlinearity and to retain some physical sight into other important nonlinearities. Besides, an asperity based interface friction model is introduced to describe the complex stick-slip-separation dynamics at the interface. An effective real-time and synchronous experimental setup is established for model identification and validation.

Acknowledgments
Authors would like to acknowledge the support of National Natural Science Foundation of China (No. 51505020).

References

[1] Zhao, C. (2011) Ultrasonic motors: technologies and applications. Springer Science & Business Media, Berlin.
[2] Fu, C., Guo, H. (2009) A study of linear ultrasonic motor. In: International Conference on Applied Superconductivity and Electromagnetic Devices, IEEE. Chengdu. pp. 104-107.
[3] Tsai, M. S., Lee, C. H., Hwang, S. H. (2003) Dynamic modeling and analysis of a bimodal ultrasonic motor. IEEE Trans. on Ultrasonic Ferroelectrics & Frequency Control, 50(3):245-256.
[4] Zhou, S., Yao, Z. (2012) Micromechanic model for contact between a linear ultrasonic motors stator and mover. Journal of Vibration and Shock, 31(20):90-93. (in Chinese)
[5] Lv, Q., Yao, Z., Li, X. (2017) Contact analysis and experimental investigation of a linear ultrasonic motor. Ultrasonics, 81:23-38.
[6] Chen, T. C., Ren, T. J., Chen, P. L., et al. (2010) Recurrent fuzzy neural network controller for linear ultrasonic motor. In: Proceedings of SICE Annual Conference. Taipei. 1786-1791.
[7] Ge, H. W., Liang, Y. C., Marchese, M. (2013) A modified particle swarm optimization-based dynamic recurrent neural network for identifying and controlling nonlinear system. Computers & Structures, 85(21):1161-1622.